Journal of Sound and Vibration 329 (2010) 1332–1347

Contents lists available at ScienceDirect

Journal of Sound and Vibration

journal homepage: www.elsevier.com/locate/jsvi

Vibrations of balanced fault-free ball bearings

S.H. Ghafari [a], E.M. Abdel-Rahman [b], F. Golnaraghi [c,*], F. Ismail [d]

[a] GCM Tech, Unit 4, 195 Clayton Drive, Markham, ON, Canada L3R 7P3
[b] Department of Systems Design Engineering, University of Waterloo, Waterloo, ON, Canada N2L 3G1
[c] Simon Fraser University, Department of Engineering Science, 8888 University Drive, Burnaby, BC, Canada V5A 1S6
[d] University of Waterloo, Department of Mechanical and Mechatronics Engineering, Waterloo, ON, Canada N2L 3G1

ARTICLE INFO

Article history:
Received 15 March 2007
Received in revised form
28 October 2009
Accepted 2 November 2009
Handling Editor: M.P. Cartmell
Available online 22 December 2009

ABSTRACT

This paper investigates the vibrations of balanced fault-free ball bearings. A lumped mass-damper-spring model is adopted including the use of the Hertzian contact theory to represent the stiffness of the bearing rolling elements. We found that the equilibrium point of the bearing undergoes a supercritical pitchfork bifurcation as the bearing internal clearance increases. We developed closed-form expressions for the frequency-response functions of the horizontal and vertical motions of bearings with small internal clearance (below the bifurcation point). We also developed a chaos map to describe the locations and intensity of chaos in the internal clearance–shaft speed parameter space for bearings with larger internal clearance (beyond the bifurcation point).

1. Introduction

As a first step in the development of a ball bearing health-monitoring system, it is essential to establish a base-line for the behaviour of healthy bearings. Gustafsson and Tallian [1] and Sunnersjo [2] identified the fundamental reason for the vibrations of rolling element bearings to be the varying compliance of the rolling elements supporting the radial load. Their studies show that the overall bearing compliance varies with a frequency corresponding to the ball-passage frequency. As a result, fault-free bearings supporting balanced shafts and rotors vibrate due to the finite number of rolling elements carrying the radial load thereby constituting self-excited oscillators. Tallian and Gustafsson [3] predicted that larger internal clearances increase the level of bearing vibrations. Wardel and Poon [4] experimentally verified this conclusion. In a series of papers, Tamura and co-workers [5–7] analyzed the stiffness characteristics and vibrations of self-aligning ball bearings for bearings containing two, three, four, and a large number of balls. They used the Hertzian contact theory to derive simplified expressions describing the nonlinear stiffness of the balls.

Meyer et al. [8] first proposed to model bearing vibrations by linear springs representing the balls under axial (thrust) loads. Tandon and Choudhury [9,10] developed a three degree-of-freedom model for the vibration of rolling element bearings to characterize and predict the bearing response to inner race, rolling element, and outer race defects under radial loads. They suggested that the stiffness of the rolling elements could be assumed linear, since variations in the shaft displacement, over time, were small. Akturk et al. [11,12] presented a nonlinear three degree-of-freedom model that used

* Corresponding author. Tel.: +1 778 782 8054; fax: +1 604 291 4951.
E-mail addresses: info@gcmtech.ca (S.H. Ghafari), eihab@uwaterloo.ca (E.M. Abdel-Rahman), mfgolnar@sfu.ca (F. Golnaraghi). fmismail@mecheng1.uwaterloo.ca (F. Ismail).

0022-460X/$ - see front matter © 2009 Elsevier Ltd. All rights reserved.
doi:10.1016/j.jsv.2009.11.003

Hertzian contact theory to represent the stiffness of the rolling elements. Numerical simulations of the model showed that increasing the preload and/or the number of balls in the bearing reduces the vibration amplitude.

Recently, there has been a lot of interest in the vibrations of faulty bearings and/or bearings supporting unbalanced radial loads. Most of that work has used two-degree-of-freedom nonlinear models employing the Hertzian contact theory to represent the stiffness of the rolling elements. For example, Tiwari et al. [13,14] studied the vibrations of fault-free ball bearings excited by unbalanced rotors for various values of internal clearance. Their numerical and experimental results showed that chaos appears in three ranges of the shaft speed. As the level of external forcing (unbalance) decreased, the shaft speed ranges where chaos happened shifted down the frequency spectrum and the extent of the chaotic response within these ranges increased. They also found that the prevalence of nonlinear phenomena in the bearing response increases as the level of external forcing and internal clearance increase. Harsha et al. [15–17] investigated the effects of surface waviness of the inner and outer races on the vibrations of ball and roller bearings. They showed that surface waviness acts as an external forcing frequency that is a rational multiple of the ball passage frequency and that increasing the number of balls reduces the vibration amplitude. Further, they confirmed the appearance of chaos in the bearing response in three ranges of the shaft speed.

A subset of research on the vibrations of ball bearings has studied the vibrations of fault-free bearings supporting balanced radial loads. The main difference between the vibrations of those bearings and the vibrations of faulty or unbalanced bearings is that the former represent a simple self-excited oscillator, while the latter represent a more complex case of multi-frequency excitation. Gad et al. [18] showed numerically that balanced fault-free ball bearings exhibit harmonic, superharmonic, subharmonic, beat, and chaotic oscillations. Mevel and Guyader [19] used numerical simulations to show that a lightly damped ball bearing undergoes a period-doubling route to chaos when the ball passage frequency is near the first critical speed (natural frequency of horizontal motion) and a quasi-periodic route to chaos when the ball passage frequency is near the second critical speed (natural frequency of vertical motion). Tiwari et al. [20] found three chaotic attractors that do not necessarily correspond to the critical shaft speeds and that those attractors shrink and disappear as the internal clearance decreases and the damping increases. They also found that the critical speeds and chaotic attractors appear at lower shaft speeds as the internal clearance increases. Harsha [21] reported a single chaotic attractor appearing through a period-doubling route to chaos at shaft speeds corresponding to the horizontal natural frequency of the vibratory system and another range of quasi-periodic motions at higher shaft speeds. Ghafari et al. [22] experimentally verified the existence of a chaotic attractor in the vibrations of balanced fault-free ball bearings.

The objective of the current work is to provide a better understanding of the vibrations of balanced fault-free ball bearings and the impact of the bearing internal clearance on those vibrations. Towards that goal, we use a nonlinear dynamic model based on the Hertzian contact theory to explore the bifurcations of the equilibrium point of the bearing, develop closed-form expressions for the self-excited motions of the bearing, and map the chaotic attractors present in the internal clearance-shaft speed parameter space.

2. Rotor-shaft-bearing system model

We investigate the dynamics of the ball bearing *in-situ* as a part of a rotor-shaft-bearing assembly. Following Fukata et al. [23], the system is modeled as a mass-damper-spring system. As illustrated in Fig. 1, the rotor and shaft are modeled

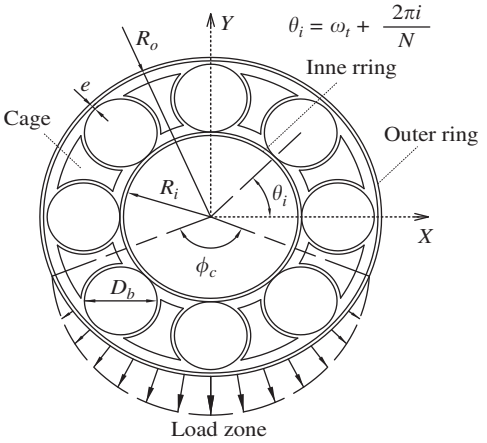

Fig. 1. Ball bearing model.

as a lump rigid mass located at the center of the inner ring (x, y), and supported by a set of identical parallel nonlinear springs representing the balls. The restoring force of the springs (balls) in the loading zone provides the excitation applied to the mass. This two degree-of-freedom model ignores the inertia of the balls and the flexibility of the shaft. Further, the following assumptions are made:

(1) The shaft is held at the center of the inner ring and the outer ring is stationary.
(2) The only external force is the weight of the rotor-shaft. The balls and raceways are fault-free and the rotor and shaft are balanced.
(3) The geometric parameters of the bearing, namely the radii of the inner R_i and outer R_o rings, the internal clearance e, and the ball diameter D_b, are constant during operation.

The cage keeps the balls equally-spaced around the shaft. The angular location of the ith ball $\theta_i(t)$ is given by:

$$\theta_i = \omega t + \frac{2\pi i}{N}, \tag{1}$$

where N is the number of balls. The cage speed ω is related to the shaft speed ω_s by

$$\omega = \frac{R_i \omega_s}{R_i + R_o}. \tag{2}$$

The restoring force $F_i(t)$ of each ball in the load zone is calculated based on Hertzian contact theory

$$F_i = k\delta_i^n, \tag{3}$$

where the stiffness k is a function of the contact curvatures, elastic modulus, and Poisson's ratio of the bearing components. The power n depends on the rolling element shape; for ball elements n=1.5. The radial deformation of each ball $\delta_i(t)$ is given by:

$$\delta_i = x\cos\left(\omega t + \frac{2\pi i}{N}\right) + y\sin\left(\omega t + \frac{2\pi i}{N}\right) - e. \tag{4}$$

Using Eqs. (3) and (4) and summing the forces in the X and Y directions, the governing equations of motion of the bearing system can be expressed as follows:

$$m\ddot{x} + c\dot{x} + k\sum_{i=0}^{N_c-1}\left(x\cos\left(\omega t + \frac{2\pi i}{N}\right) + y\sin\left(\omega t + \frac{2\pi i}{N}\right) - e\right)^{1.5}\cos\left(\omega t + \frac{2\pi i}{N}\right) = 0,$$

$$m\ddot{y} + c\dot{y} + k\sum_{i=0}^{N_c-1}\left(x\cos\left(\omega t + \frac{2\pi i}{N}\right) + y\sin\left(\omega t + \frac{2\pi i}{N}\right) - e\right)^{1.5}\sin\left(\omega t + \frac{2\pi i}{N}\right) = W, \tag{5}$$

where $x(t)$ and $y(t)$ are the coordinates of the shaft mass, $N_c(t)$ is the number of balls in the loading zone, W is the weight of the rotor and shaft, and c is the overall damping coefficient.

2.1. The loading zone

The balls are compressed as they transmit the radial load from the inner ring to the outer ring. For bearings with nonzero radial clearance, the radial load is distributed over a subset of the balls, Fig. 2, inside a load-carrying zone. The

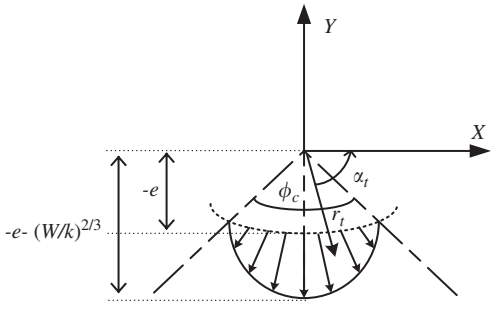

Fig. 2. Load distribution angle.

number of those balls N_c is a function of the load, radial clearance, and the dynamic state of the bearing. The radial deformation of the balls is positive *only* for those balls within the loading zone

$$\begin{cases} \delta_i > 0 & i\text{th ball inside the load zone.} \\ \delta_i \le 0 & i\text{th ball outside the load zone.} \end{cases} \tag{6}$$

Applying the polar transformation $x=r_t\cos\alpha_t$, $y=r_t\sin\alpha_t$ to Eq. (4) and using condition (6), we find that the balls in the load zone must satisfy the following condition

$$\cos\left(\omega t+\frac{2\pi i}{N}-\alpha_t\right)\ge\frac{e}{r_t}. \tag{7}$$

The extreme excursion $ext(r_t)$ occurs when a single ball is carrying the weight of the rotor and shaft. For a quasi-static shaft $\omega_s\approx 0$ and using Hertzian contact theory, that value is

$$ext(r_t)=e+\left(\frac{W}{k}\right)^{2/3}. \tag{8}$$

Substituting this value in Eq. (7) yields the load distribution angle

$$\phi_c=2\cos^{-1}\frac{e}{e+(W/k)^{2/3}}. \tag{9}$$

The number of balls inside the loading zone can then be found from

$$N_c=\frac{N}{\pi}\cos^{-1}\frac{e}{e+(W/k)^{2/3}}. \tag{10}$$

We note that for a dynamic case $\omega_s\neq 0$, the number of balls in the loading zone N_c and their locations within the zone will change with time, thereby changing the system stiffness. This is the underlying source of vibrations and the time varying nature of the system.

3. Equilibrium points

The equilibrium points of the shaft, denoted (x_e, y_e), are any set for which the time derivatives in the equations of motion, Eq. (5), are identically zero

$$\begin{aligned} &\sum_{i=0}^{N_c-1}\left(x_e\cos\left(\omega t+\frac{2\pi i}{N}\right)+y_e\sin\left(\omega t+\frac{2\pi i}{N}\right)-e\right)^{1.5}\cos\left(\omega t+\frac{2\pi i}{N}\right)=0,\\ &\sum_{i=0}^{N_c-1}\left(x_e\cos\left(\omega t+\frac{2\pi i}{N}\right)+y_e\sin\left(\omega t+\frac{2\pi i}{N}\right)-e\right)^{1.5}\sin\left(\omega t+\frac{2\pi i}{N}\right)=\frac{W}{k}. \end{aligned} \tag{11}$$

The location of the equilibrium points depends on the clearance e, radial force W, and the number of balls in the loading zone N_c.

The maximum number of balls inside the loading zone $N/2$ occurs when there is no internal clearance $e=0$. In this case and for a quasi-static shaft $\omega_s\approx 0$, we find, (developed in Appendix A), that for an even number of balls $N\ge 8$ there is a single equilibrium point located at $(x_e,y_e)|_{e=0}=(0,-(4W/Nk)^{2/3})$.

In order to study the bifurcations of the equilibrium point as the internal clearance increases $e>0$, we solved Eq. (11) numerically for ball bearings SKF6204 with the specifications listed in Table 1. First, the equilibrium points were obtained under a quasi-static condition $\omega_s\approx 0$. The number of balls in the loading zone was found to vary between four and one depending on the amount of internal clearance. Fig. 3 shows the location of the equilibrium points in the X–Y plane.

When the internal clearance was less than $e<4.5\,\mu$m, the inner ring was in contact with 3 or 4 balls and a single equilibrium point existed. As the internal clearance increased beyond $e=4.5\,\mu$m, three coexisting equilibrium points appeared. We characterize the stability of those points by evaluating the eigenvalues of the Jacobian matrix of the static

Table 1
Specification of ball bearing SKF 6204.

Ball diameter (mm)	7.938	Race groove radius (mm)	4.1278
Inner race diameter (mm)	25.5620	Number of balls	8
Outer race diameter (mm)	41.4380	Rotor-shaft weight (N)	23.004
Pitch diameter (mm)	33.5	Coefficient of stiffness (N/m$^{1.5}$)	9.21×10^9

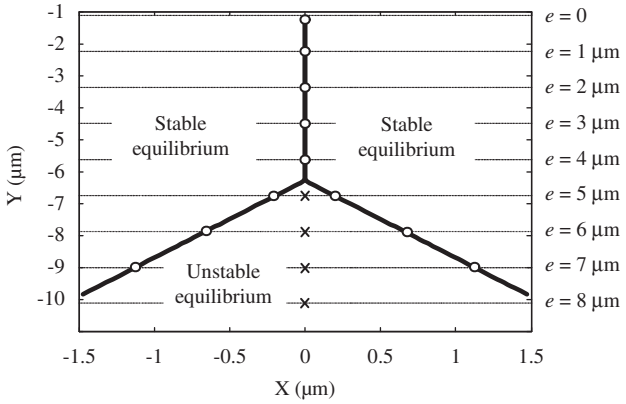

Fig. 3. Equilibrium points when $\omega_s \approx 0$. The locations are marked (o) where the point is a node and (x) where the point is a saddle.

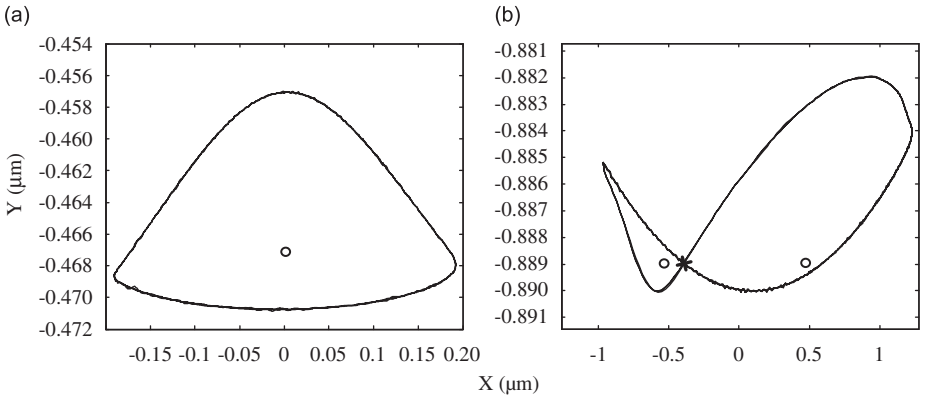

Fig. 4. Orbits the inner ring center at (a) e=3 μm and (b) e=5 μm when $\omega = 100$ rpm (o: node, x: saddle).

equilibrium equations, Eq. (11), at each equilibrium point (x_e, y_e)

$$J = \begin{bmatrix} 0 & 1 & 0 & 0 \\ \frac{-k}{m}\sum_{i=0}^{N_c-1} 1.5(x_e\cos\theta_i + y_e\sin\theta_i - e)^{0.5}\cos^2\theta_i & -\frac{c}{m} & \frac{-k}{m}\sum_{i=0}^{N_c-1} 1.5(x_e\cos\theta_i + y_e\sin\theta_i - e)^{0.5}\cos^2\theta_i\sin\theta_i & 0 \\ 0 & 0 & 0 & 1 \\ \frac{-k}{m}\sum_{i=0}^{N_c-1} 1.5(x_e\cos\theta_i + y_e\sin\theta_i - e)^{0.5}\cos^2\theta_i\sin\theta_i & 0 & \frac{-k}{m}\sum_{i=0}^{N_c-1} 1.5(x_e\cos\theta_i + y_e\sin\theta_i - e)^{0.5}\sin^2\theta_i & -\frac{c}{m} \end{bmatrix}. \quad (12)$$

The Jacobian matrix generates four complex eigenvalues with negative real parts for all of the equilibrium points in the range $0 \le e \le 4.5$ μm confirming their stability. In the range of $e > 4.5$ μm, the equilibrium point closest to the Y-axis is unstable with two real eigenvalues having opposite signs and the equilibrium points away from the Y-axis is stable with all four eigenvalues having negative real parts. These results show that the equilibrium point undergoes a supercritical pitchfork bifurcation at e=4.5 μm for that bearing.

The motions of the shaft shown Fig. 4 were obtained from long-time integration of Eq. (5) for a cage speed of ω=100 rpm and two internal clearance values below and above the pitchfork bifurcation. The damping coefficient c=572.4 N s/m was measured experimentally using an impact test. Fig. 4(a) shows that the equilibrium point is a *node* with a closed symmetric orbit below the bifurcation. Beyond the bifurcation point $e > 4.5$ μm, the symmetry of the orbit is broken, Fig. 4(b), and two-potential wells appear around the two *nodes* separated by the *saddle*.

For the dynamic case $\omega_s \neq 0$, the nonlinear algebraic system of equations in (11) is solved using Newton–Raphson method for the unknowns (x_e, y_e) at discrete points in time. Where more than one equilibrium point is available, the initial guess used to start the numerical routine is varied away from the centerline of the bearing (x=0) until all possible solutions are obtained.

For internal clearance values below the bifurcation point, e=4.5 μm, the results are unchanged with a single stable equilibrium point (node) located at the Y-axis. When the internal clearance increases past the bifurcation point, the solution of Eq. (11) results in three equilibrium points with similar characteristics to those found in the quasi-static case at *each* point in time. As a result, the locations of the three equilibrium points vary with time over different stretches of a

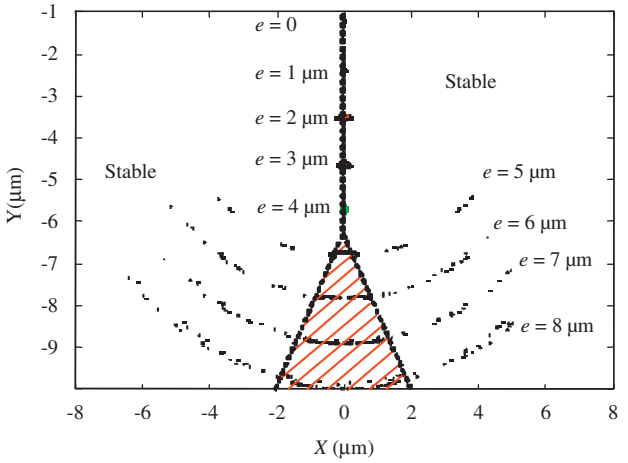

Fig. 5. Locations of the dynamic equilibrium points at ω=800 rpm. Points in the hatched area are saddles.

curve rather than exist at discrete locations. Each clearance value has its own equilibrium curve as shown in Fig. 5 for a cage speed of ω=800 rpm. These curves are symmetric with respect to the Y-axis. As the shaft rotates, the saddle moves on the center stretch of the curve, while each of the nodes move on one of the outer stretches.

The bifurcation point at e=4.5 μm separates two qualitatively different types of bearing vibrations. For small internal clearances $e < 4.5$ μm, below the bifurcation point, the self-excited vibrations are regular, symmetric, and periodic. Beyond the bifurcation point a 'two-well potential' system develops [24]. At low shaft speeds, the motions are asymmetric, periodic, and confined to one of the two wells (occurring on one side of the Y-axis only). Once the shaft speed is high enough for the self-excited oscillator to provide the necessary energy, the shaft starts jumping from one well to the other in a chaotic manner; that is: periodic excitation at a single frequency ω leading to random-like motions of the shaft with a broad spectrum of frequencies. As a result, the locations of the nodes and saddles travel *randomly* back and forth along the equilibrium curve as the shaft orbits in the phase space. This is the underlying source of the asymmetric (tailed) and net-like structure of the shaft orbits observed by Tiwari et al. [20] at low shaft speeds. At higher shaft speeds, chaos disappears and a periodic motion encompassing both wells, Fig. 4(b), appears.

4. Periodic vibrations

4.1. Analytical solution

To obtain a closed-form expression for the response of the bearing, the equations of motion, Eq. (5), are simplified by expanding the x- and y-components of the restoring force in Taylor-series around the equilibrium point. This approximation is valid only for motions in the neighbourhood of a single equilibrium point (one-well oscillations). Figs. 6 and 7 show the steady-state response of the full model compared with first-, second-, and third-order approximations when the internal clearance is equal to 0 and 4 μm, respectively.

For zero clearance e=0, the error in the response obtained using all three levels of approximation is negligible at low ω=7.5 rpm and high ω=750 rpm cage speeds. For higher values of the internal clearance e=4 μm, Fig. 7, the second and third-order approximations are more accurate than the first-order approximation. However, the steady-state error of the first-order approximation is less than 0.2% at a cage speed of ω=4800 rpm. Therefore, the first-order expansion of the equations of motion

$$\ddot{x}+\mu\dot{x}+\alpha_{11}x+\alpha_{12}y=f_x,$$

$$\ddot{y}+\mu\dot{y}+\alpha_{21}x+\alpha_{22}y=f_y+W/m, \tag{13}$$

will be adopted for the internal clearance range of $0 \le e \le 4.5$ μm and for x_e=0, where only one-well oscillations are present. The parameters μ, $\alpha_{mn}(t)$, $f_x(t)$ and $f_y(t)$ are defined by:

$$\mu = c/m,$$

$$f_x = \frac{k}{m}\sum_{i=0}^{N_c-1}\sqrt{y_e\sin\theta_i - e}\,(0.5y_e\sin\theta_i\cos\theta_i + e\cos\theta_i),$$

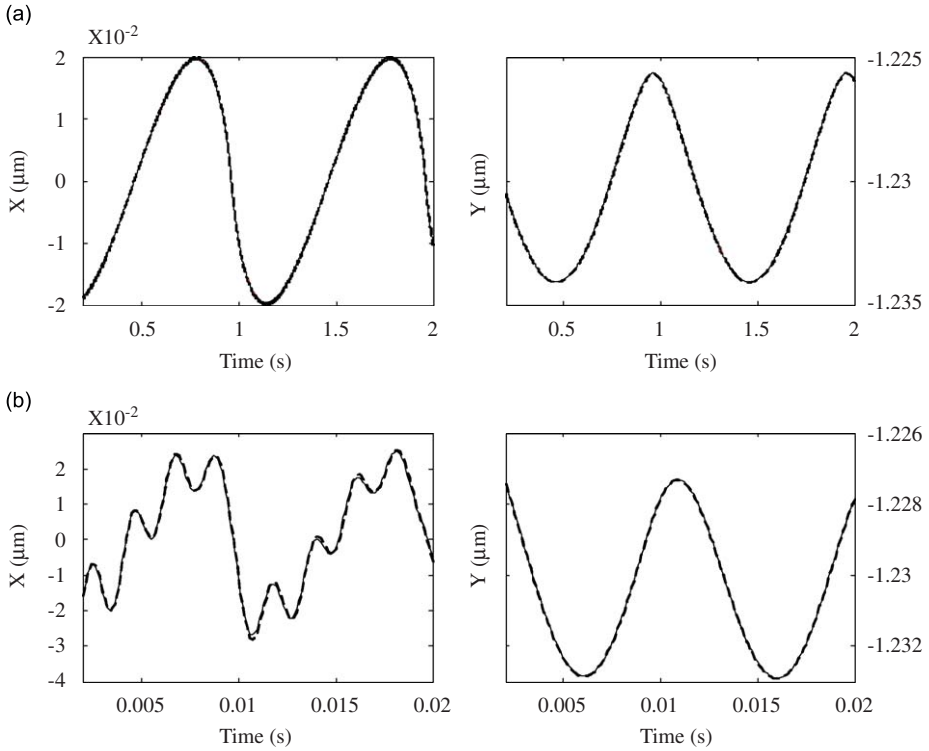

Fig. 6. Comparison between the full model (solid line) and first-, second-, and third-order approximations for e=0 and cage speeds of (a) ω=7.5 rpm, and (b) ω=750 rpm.

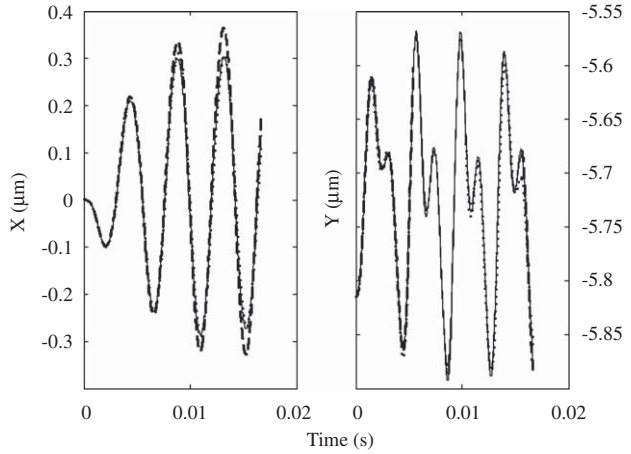

Fig. 7. Comparison between the full model (solid line) and first-order (dashed line), second-order (dotted line), and third-order (dashed-dotted line) approximations for e=4 μm and ω=4800 rpm.

$$f_y = \frac{k}{m}\sum_{i=0}^{N_c-1}\sqrt{y_e \sin\theta_i - e}(0.5y_e \sin^2\theta_i + e\sin\theta_i),$$

$$\alpha_{11} = \frac{3k}{2m}\sum_{i=0}^{N_c-1}\sqrt{y_e \sin\theta_i - e}\cos^2\theta_i \alpha_{22} = \frac{3k}{2m}\sum_{i=0}^{N_c-1}\sqrt{y_e \sin\theta_i - e}\sin^2\theta_i,$$

$$\alpha_{12} = \alpha_{21} = \frac{3k}{2m}\sum_{i=0}^{N_c-1}\sqrt{y_e \sin\theta_i - e}\cos\theta_i \sin\theta_i. \tag{14}$$

The generalized method of averaging [25] is utilized to solve the coupled linear time-varying differential system in Eq. (13) for two cases:

(1) ball bearings with zero internal clearance,
(2) ball bearings with a small radial clearance $0 \le e \le 4.5\,\mu$m.

4.1.1. Case 1: zero clearance, e=0 μm

In this case, the loading zone angle is $\phi_c=\pi$ and the number of load bearing elements is $N_c=N/2$. To further simplify the equations of motion, curve fitting is used to replace the parameters of Eq. (14) as follows:

$$f_x \equiv c_x \sin N\omega t,$$

$$f_y \equiv c_{0y} + c_y \cos N\omega t,$$

$$\alpha_{11} \equiv \sigma_x^2 + c_{11}\sin^2 N\omega t = \left(\sigma_x^2 + \frac{c_{11}}{2}\right) - \frac{c_{11}}{2}\sin 2N\omega t, \tag{15}$$

$$\alpha_{12} \equiv c_{12}\sin N\omega t \alpha_{22} \equiv \sigma_y^2 + c_{22}\cos N\omega t,$$

where

$$\sigma_x = 1.12312\sqrt{\frac{k}{m}}\sqrt[4]{y_e},$$

$$\sigma_y = 1.66174\sqrt{\frac{k}{m}}\sqrt[4]{y_e}, \tag{16}$$

and the coefficients c_{mn} are determined through curve fitting. Fig. 8 shows the time-varying parameters of Eq. (14) and their approximation using Eq. (15) for one revolution of the cage. The figures show that the curve-fitted functions and the original parameters are in good agreement.

Time t is normalized using the following parameters:

$$t_1 = \sigma_x t \quad t_2 = \sigma_y t,$$

$$2\xi_1\sigma_x = \mu \quad 2\xi_2\sigma_y = \mu. \tag{17}$$

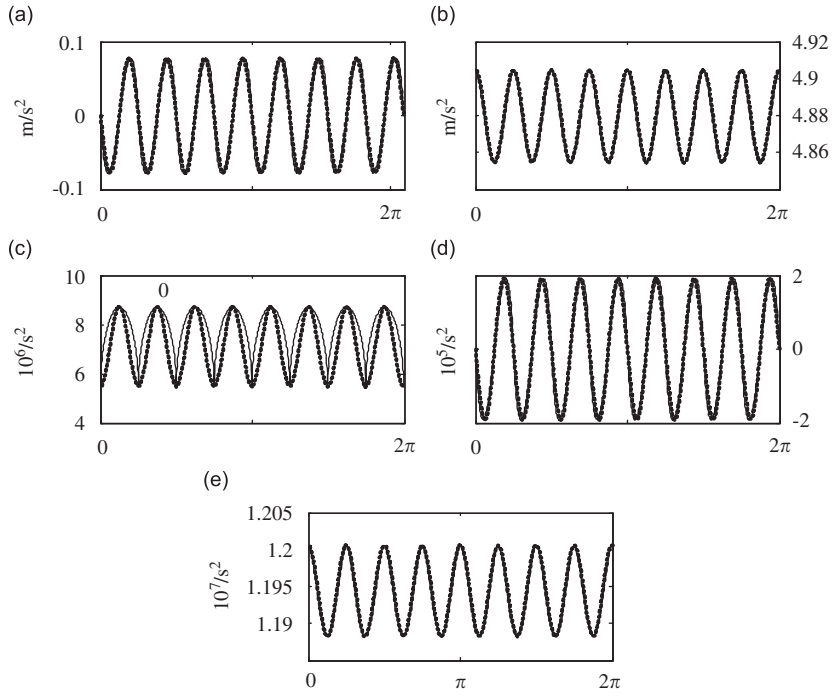

Fig. 8. The parameters (a) f_x, (b) f_y, (c) α_{11}, (d) α_{12} and α_{21}, and (e) α_{22} (solid lines) of Eq. (13) and their approximations (dotted lines) in Eq. (15).

Therefore

$$\omega_1 = \frac{N\omega}{\sigma_x} \quad \omega_2 = \frac{N\omega}{\sigma_y},$$

$$\frac{dx}{dt} = \sigma_x \frac{dx}{dt_1} \quad \frac{dy}{dt} = \sigma_y \frac{dy}{dt_2},$$

$$\frac{d^2x}{dt^2} = \sigma_x^2 \frac{d^2x}{dt_1^2} \quad \frac{d^2y}{dt^2} = \sigma_y^2 \frac{d^2y}{dt_2^2}.$$

Using the normalized parameters in Eq. (13) yields

$$\ddot{x} + 2\xi_1\dot{x} + \left(1 + \frac{c_{11}\sin^2\omega_1 t_1}{\sigma_x^2}\right)x + \left(\frac{c_{12}\cos\omega_1 t_1}{\sigma_x^2}\right)y - \frac{c_x \sin\omega_1 t_1}{\sigma_x^2} = 0,$$

$$\ddot{y} + 2\xi_2\dot{y} + \left(\frac{c_{21}\sin\omega_2 t_2}{\sigma_y^2}\right)x + \left(1 + \frac{c_{22}\cos\omega_2 t_2}{\sigma_y^2}\right)y - \frac{c_y\cos\omega_2 t_2}{\sigma_y^2} - \left(\frac{mc_{0y}+W}{m\sigma_y^2}\right) = 0. \tag{18}$$

We use the method of variation of parameters to obtain solutions for Eq. (18) when the ball passage speed is in the neighbourhood of the natural frequency of horizontal shaft motions ($N\omega \approx \omega_1$) and in the neighbourhood of the natural frequency of vertical motion shaft ($N\omega \approx \omega_2$).

The horizontal and vertical natural frequencies ω_1 and ω_2 are incommensurate ($p\ \sigma_x \neq q\ \sigma_y$) and far from each other. Therefore, in the vicinity of the natural frequency and in the presence of damping we can decouple the steady-state motions in the horizontal and vertical directions, since the motions in the non-resonant direction will decay over time. Consequently, the bearing response can be represented using a single degree of freedom in each of the sub-cases ($N\omega \approx \omega_1$) and ($N\omega \approx \omega_2$):

$$x = u_1\cos(\omega_1 t_1 + \gamma_1), \dot{x} = -\omega_1 u_1 \sin(\omega_1 t_1 + \gamma_1),$$

$$y = u_2\cos(\omega_2 t_2 + \gamma_2), \dot{y} = -\omega_2 u_2 \sin(\omega_2 t_2 + \gamma_2). \tag{19}$$

Letting $\omega_1 t_1 + \gamma_1 = \varphi$ and $\omega_2 t_2 + \gamma_2 = \psi$, and substituting Eq. (19) into (18) we get the following set of equations

$$\dot{u}_1 = -u_1\omega_1 \sin\varphi\cos\varphi - 2\xi_1 u_1 \sin^2\varphi + \left(1 + \frac{c_{11}\sin^2(\varphi-\gamma_1)}{\sigma_x^2}\right)\frac{u_1\sin\varphi\cos\varphi}{\omega_1} + \frac{u_2 c_{12}\cos(\varphi-\gamma_1)\sin\varphi\cos\psi}{\omega_1\sigma_x^2} - \frac{c_x\sin(\varphi-\gamma_1)\sin\varphi}{\omega_1\sigma_x^2},$$

$$\dot{\gamma}_1 = -\omega_1\cos^2\varphi - 2\xi_1\cos\varphi\sin\varphi + \left(1 + \frac{c_{11}\sin^2(\varphi-\gamma_1)}{\sigma_x^2}\right)\frac{u_1\cos^2\varphi}{\omega_1} + \frac{u_2 c_{12}\cos(\varphi-\gamma_1)\cos\varphi\cos\psi}{u_1\omega_1\sigma_x^2} - \frac{c_x\sin(\varphi-\gamma_1)\cos\varphi}{u_1\omega_1\sigma_x^2}. \tag{20}$$

$$\dot{u}_2 = -u_2\omega_2\sin\psi\cos\psi - 2\xi_2 u_2\sin^2\psi + \frac{c_{21}\sin(\psi-\gamma_2)u_1\sin\psi\cos\varphi}{\omega_2\sigma_y^2} + \left(1 + \frac{c_{22}\cos(\psi-\gamma_2)}{\sigma_y^2}\right)\frac{u_2\sin\psi\cos\psi}{\omega_2} - \frac{c_y\cos(\psi-\gamma_2)\sin\psi}{\omega_2\sigma_y^2} - \frac{(mc_{0y}+W)\sin\psi}{m\omega_2\sigma_y^2},$$

$$\dot{\gamma}_2 = -\omega_2\cos^2\psi - 2\xi_2\cos\psi\sin\psi + \frac{u_1 c_{21}\sin(\psi-\gamma_2)\cos\psi\cos\varphi}{u_2\omega * \sigma_y^2} + \left(1 + \frac{c_{22}\cos(\psi-\gamma_2)}{\sigma_y^2}\right)\frac{\cos^2\psi}{\omega_2} - \frac{c_y\cos(\psi-\gamma_2)\cos\psi}{u_2\omega_2\sigma_y^2} - \frac{(mc_{0y}+W)\cos\psi}{m\omega_2 u_2\sigma_y^2}. \tag{21}$$

Using Kryolov–Bogoliubov first approximation, the right hand-side of Eqs. (20) and (21) can be averaged for one period over φ and ψ, respectively, to produce the modulation equations for the sub-case ($N\omega \approx \omega_1$)

$$\dot{u}_1 = \xi_1 u_1 - \frac{u_1 c_{11}\sin 2\gamma_1}{8\omega_1\sigma_x^2} - \frac{c_x\cos\gamma_1}{2\omega_1\sigma_x^2},$$

$$\dot{\gamma}_1 = -\frac{\omega_1}{2} - \frac{c_{11}\cos 2\gamma_1}{8\omega_1\sigma_x^2} + \frac{c_x\sin\gamma_1}{2u_1\omega_1\sigma_x^2} + \frac{2\sigma_x^2 + c_{11}}{4\omega_1\sigma_x^2}. \tag{22}$$

And the sub-case ($N\omega \approx \omega_2$)

$$\dot{u}_2 = -\xi_1 u_2 - \frac{c_y\sin\gamma_2}{2\omega_2\sigma_y^2},$$

$$\dot{\gamma} = \frac{\omega_2}{2} + \frac{1}{2\omega_2} - \frac{c_y\cos\gamma_2}{2u_2\omega_2\sigma_y^2}. \tag{23}$$

To study the steady-state response of the system, the fixed points of each set of modulation equations are found by setting right hand-sides of Eqs. (22) and (23) equal to zero and assuming $c_{11}u_1 \ll 4c_x$. We obtain the frequency-response functions for the horizontal and vertical bearing motions in closed-form as

$$u_1 = \frac{c_x}{2\sigma_x^2\sqrt{(\xi_1\omega_1)^2+\left(\frac{\omega_1^2}{2}-\frac{2\sigma_x^2+c_{11}}{4\sigma_x^2}\right)^2}}, \tag{24}$$

and

$$u_2 = \frac{c_y}{2\sigma_y^2\sqrt{(\xi_2\omega_2)^2+\left(\frac{\omega_2^2}{2}-\frac{1}{2}\right)^2}}. \tag{25}$$

4.1.2. Case 2: a small clearance (e=4 μm)

In this case, the number of balls in the loading zone can be obtained from Eq. (10). In order to apply the method of averaging, the square root term in Eq. (14) is approximated as follows:

$$\sqrt{y_e\sin\theta_i - e} \approx \frac{y_e}{2\sqrt{e}}\sin^2\theta_i. \tag{26}$$

Fig. 9 shows that this approximation is valid within a limited range of the period when ball number i is in the loading zone. Outside that range, the approximate function is set equal to zero since the ball is not applying force to the shaft.

Time, in the simplified equations of motion, Eq. (13), is normalized according to Eq. (17), therefore we can write

$$\omega_1 = \frac{\omega}{\sigma_x}\omega_2 = \frac{\omega}{\sigma_y} \tag{27}$$

and obtain

$$\begin{aligned}&\ddot{x}+2\xi_1\dot{x}+\left(\frac{3ky_e}{4\sqrt{e}m\sigma_x^2}\sum_{i=0}^{N_c-1}\sin^2\theta_i\cos^2\theta_i\right)x+\left(\frac{3ky_e}{4\sqrt{e}m\sigma_x^2}\sum_{i=0}^{N_c-1}\sin^3\theta_i\cos\theta_i\right)y-\frac{ky_e}{2\sqrt{e}m\sigma_x^2}\sum_{i=0}^{N_c-1}\sin^2\theta_i(0.5y_e\sin\theta_i\cos\theta_i+e\cos\theta_i)\\ &=0\ddot{y}+2\xi_2\dot{y}+\left(\frac{3ky_e}{4\sqrt{e}m\sigma_y^2}\sum_{i=0}^{N_c-1}\sin^3\theta_i\cos\theta_i\right)x+\left(\frac{3ky_e}{4\sqrt{e}m\sigma_y^2}\sum_{i=0}^{N_c-1}\sin^4\theta_i\right)y-\frac{ky_e}{2\sqrt{e}m\sigma_y^2}\sum_{i=0}^{N_c-1}\sin^2\theta_i(0.5y_e\sin^2\theta_i+e\sin\theta_i)=\frac{W}{m}.\end{aligned} \tag{28}$$

Using the method of variation of parameters, we obtain solutions of Eq. (28) for the sub-cases treated in the previous subsection: ($N\omega \approx \omega_1$) and ($N\omega \approx \omega_2$). Following a similar argument, we decouple the motions in the horizontal and vertical directions and use the one-mode approximations assumed in Eq. (19). Using Eq. (19) in (28), we transform them to the first-order form

$$\dot{u}_1 = -u_1\omega_1\sin\varphi\cos\varphi - 2\xi_1u_1\sin^2\varphi + \frac{3u_1ky_e}{4\sqrt{e}m\omega_1\sigma_x^2}\sum_{i=0}^{N_c-1}\sin^2(\varphi_i-\gamma_1)\cos^2(\varphi_i-\gamma_1)\sin\varphi\cos\varphi + \frac{3u_2ky_e}{4\omega_1\sqrt{e}m\sigma_x^2}$$

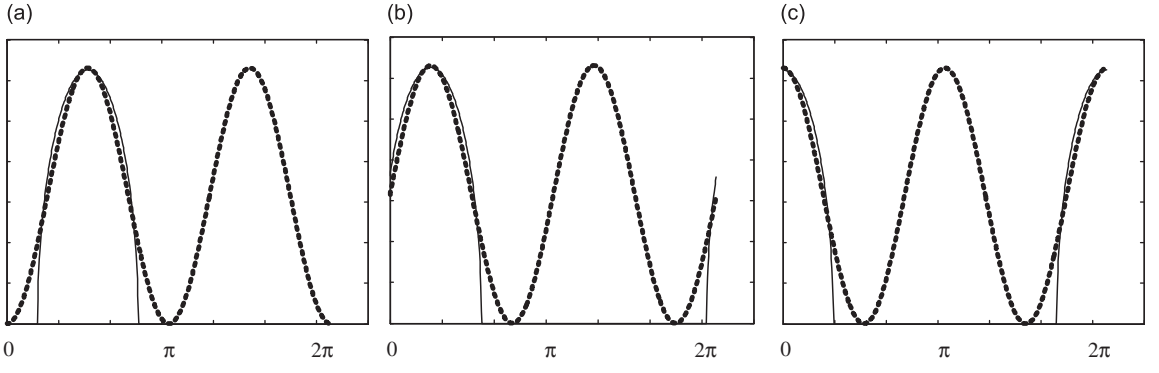

Fig. 9. Plots of the full model (solid lines) and approximate (dotted lines) functions of Eq. (26). For ball number (a) i=0 the valid range is [0, π], (b) i=1 the valid range is [0, (3/4)π]∪[(7/4)π, 2π], and (c) i=2 the valid range is [0, (1/2)π]∪[(3/4)π, 2π].

$$\sum_{i=0}^{N_c-1}\sin^3(\varphi_i-\gamma_1)\cos(\varphi_i-\gamma_1)\sin\varphi\cos\psi-\frac{ky_e}{2\sqrt{e}m\omega_1\sigma_x^2}\sum_{i=0}^{N_c-1}\sin^2(\varphi-\gamma_1)(0.5y_e\sin(\varphi_i-\gamma_1)\cos(\varphi_i-\gamma_1)+e\cos(\varphi_i-\gamma_1))\sin\varphi.$$

$$\dot{\gamma}_1=-\omega_1\cos^2\varphi-2\xi_1\sin\varphi\cos\varphi+\frac{3ky_e}{4\sqrt{e}m\omega_1\sigma_x^2}\sum_{i=0}^{N_c-1}\sin^2(\varphi_i-\gamma_1)\cos^2(\varphi_i-\gamma_1)\cos^2\varphi+\frac{3u_2ky_e}{4\omega_1u_1\sqrt{e}m\sigma_x^2}$$
$$\sum_{i=0}^{N_c-1}\sin^3(\varphi_i-\gamma_1)\cos(\varphi_i-\gamma_1)\cos\varphi\cos\psi-\frac{ky_e}{2\sqrt{e}m\omega_1u_1\sigma_x^2}\sum_{i=0}^{N_c-1}\sin^2(\varphi-\gamma_1)(0.5y_e\sin(\varphi_i-\gamma_1)\cos(\varphi_i-\gamma_1)+e\cos(\varphi_i-\gamma_1))\cos\varphi \tag{29}$$

and

$$\dot{u}_2=-u_2\omega_2\sin\psi\cos\psi-2\xi_2u_2\sin^2\psi+\frac{3u_1ky_e}{4\sqrt{e}m\omega_2\sigma_y^2}\sum_{i=0}^{N_c-1}\sin^3(\psi_i-\gamma_2)\cos(\psi_i-\gamma_2)\sin\psi\cos\varphi+\frac{W\sin\psi}{m\omega_2\sigma_y^2}$$
$$+\frac{3u_2ky_e}{4\omega_2\sqrt{e}m\sigma_y^2}\sum_{i=0}^{N_c-1}\sin^4(\psi_i-\gamma_2)\sin\psi\cos\psi-\frac{ky_e}{2\sqrt{e}m\omega_2\sigma_y^2}\sum_{i=0}^{N_c-1}\sin^2(\psi_i-\gamma_2)(0.5y_e\sin^2(\psi_i-\gamma_2)+e\sin(\psi_i-\gamma_2))\sin\psi,$$

$$\dot{\gamma}_2=-\omega_2\cos^2\psi-2\xi_2\sin\psi\cos\psi+\frac{3u_1ky_e}{4\sqrt{e}m\omega_2\sigma_y^2}\sum_{i=0}^{N_c-1}\sin^3(\psi_i-\gamma_2)\cos(\psi_i-\gamma_2)\cos\psi\cos\varphi+\frac{W\cos\psi}{m\omega_2u_2\sigma_y^2}$$
$$+\frac{3ky_e}{4\omega_2\sqrt{e}m\sigma_y^2}\sum_{i=0}^{N_c-1}\sin^4(\psi_i-\gamma_1)\cos^2\psi-\frac{ky_e}{2\sqrt{e}m\omega_2u_2\sigma_y^2}\sum_{i=0}^{N_c-1}\sin^2(\psi_i-\gamma_2)(0.5y_e\sin^2(\psi_i-\gamma_2)+e\sin(\psi_i-\gamma_2))\cos\psi. \tag{30}$$

Averaging the right hand-side of Eqs. (29) and (30) over the range where each ball is in the loading zone results in two sets of modulation equations representing the decoupled horizontal u_1 and vertical u_2 resonant responses

$$\dot{u}_1=-u_1\xi_1+\frac{C_1}{\omega_1}(\sin\gamma_1+\cos\gamma_1),$$

$$\dot{\gamma}_1=-\frac{\omega_1}{2}+\frac{C_2}{\omega_1}-\frac{C_1}{u_1\omega_1}(\sin\gamma_1-\cos\gamma_1), \tag{31}$$

and

$$\dot{u}_2=-u_2\xi_2+\frac{C_3u_2}{\omega_2}\cos2\gamma_2-\frac{C_4}{\omega_2}(-\sin\gamma_2+\cos\gamma_2),$$

$$\dot{\gamma}_2=-\frac{\omega_2}{2}+\frac{0.28C_3}{\omega_2}+\frac{C_3}{\omega_2}\sin2\gamma_2-\frac{C_4}{u_2\omega_2}(-\sin\gamma_2-\cos\gamma_2), \tag{32}$$

where

$$C_1=\frac{0.1067ky_e}{2\sqrt{e}m\sigma_x^2}C_3=\frac{0.1875ky_2}{4\sqrt{e}m\sigma_y^2},$$

$$C_2=\frac{0.273ky_e}{4\sqrt{e}m\sigma_x^2}C_4=\frac{0.3201ky_e\sqrt{e}}{2m\sigma_y^2}. \tag{33}$$

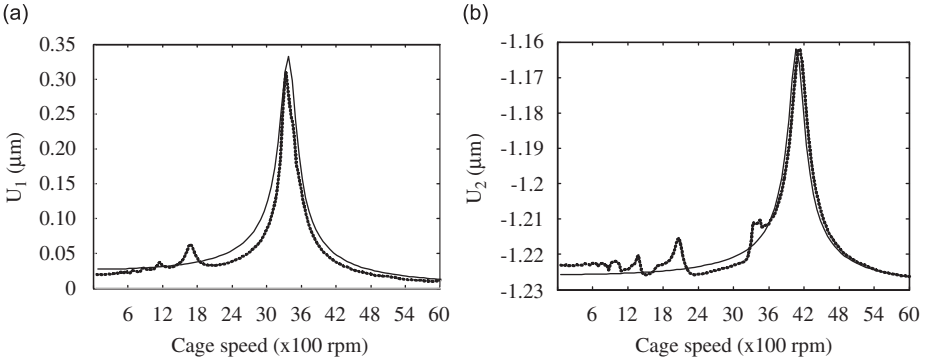

Fig. 10. The analytical (solid lines) and numerical (dotted lines) frequency-response curves of the (a) horizontal and (b) vertical shaft motions for $e=0\,\mu m$.

To find the steady-state response, we set the left hand-side of each set of modulation equations equal to zero and assume that $C_3\ u_2 \ll C_4$ to obtain the frequency-response functions of the horizontal and vertical bearing motions

$$u_1 = \frac{\sqrt{2}C_1}{\sqrt{(\xi_1\omega_1)^2 + \left(\frac{\omega_1^2}{2} - C_2\right)^2}}$$

$$u_2 = \frac{\sqrt{2}C_4}{\sqrt{(\xi_2\omega_2)^2 + \left(\frac{\omega_2^2}{2} - 0.28C_3\right)^2}}. \tag{34}$$

4.2. Comparison of analytical and numerical solutions

Fig. 10 compares the frequency-response curves of the horizontal u_1 and vertical u_2 motions obtained using the method of averaging to those obtained using numerical integration of the full model, Eq. (5), for ball bearing SKF6204. There is good agreement between the analytical and numerical responses. However, the quality of the approximation deteriorates in the neighbourhood of the superharmonic resonance of order one-half, $1/2\omega_1$ and $1/2\omega_2$, of the vertical and horizontal motions and in the neighbourhood of primary resonance ω_1 of the vertical motion. The reason for the former discrepancy is the underlying assumption, in Eq. (19), that the balls are responding to primary-resonance excitations in the neighbourhood of the natural frequency ω_1 or ω_2. As the frequency of excitations move away from these neighbourhoods, the quality of the approximation degrades. The reason for the latter discrepancy is that our approximate solution, Eq. (23), ignores the coupling between the horizontal and vertical modes of vibration.

Fig. 11 compares the frequency-response of the horizontal and vertical shaft motions obtained analytically to those obtained numerically for ball bearing SKF6204. Fig. 11(a) shows good agreement between the two sets of results indicating that the analytical solution is a good approximation of the horizontal motions throughout the range of frequency. The quality of the approximation deteriorates for vertical shaft motions, Fig. 11(b), especially in the neighbourhood of the natural frequency of the horizontal motions ω_1 and its superharmonic and subharmonic resonances. This is expected since the basic assumption, Eq. (19), that the vertical and horizontal motions can be decoupled is violated in these ranges of excitation. These results indicate that for small non-zero internal clearance, the energy transferred from the vertical to the

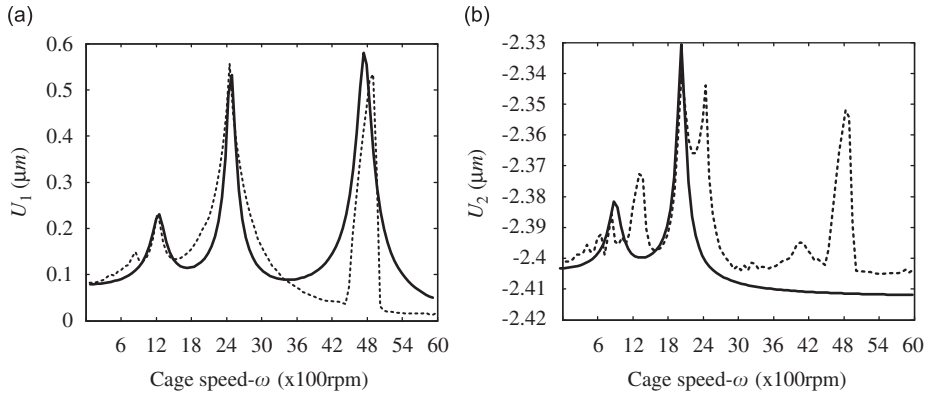

Fig. 11. The analytical (solid lines) and numerical (dotted lines) frequency-response curves of the (a) horizontal and (b) vertical shaft motions for $e = 4\ \mu m$.

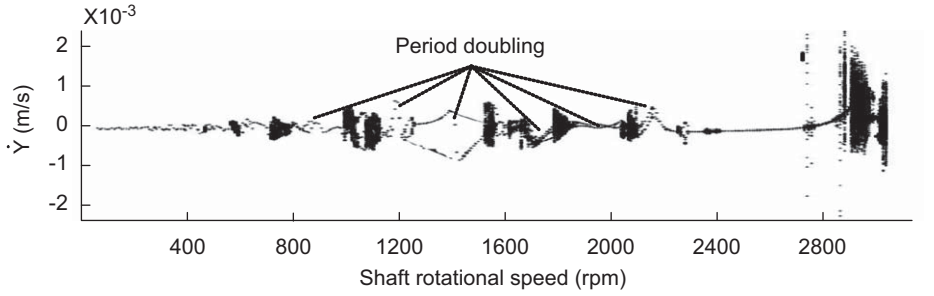

Fig. 12. The bifurcation diagram of the bearing vibration when $e = 7\ \mu m$.

horizontal motions of the shaft is small and can be ignored, but the energy transferred from the horizontal to the vertical motions is significant and cannot be ignored. This is in agreement with Tiwari et al. [14] experimental finding of cross-coupling between the vertical and horizontal natural frequencies in ball bearings.

Comparing the frequency-response curves at zero clearance, Fig. 10, and small positive clearance, Fig. 11, shows that increasing the internal clearance lowers the vertical and horizontal natural frequencies. As a result, bearings with larger internal clearances will experience resonance at lower shaft speeds. This result is in agreement with the experimental and analytical results of Tiwari et al. [14,20]. The reason for this *softening* effect is the decrease in the 'average' number of balls supporting the rotor-shaft weight over a single period as the clearance increases which decreases the 'effective' linear stiffness of the oscillator. This effect is more pronounced in the vertical than in the horizontal direction. In fact, the order of the natural frequencies of the bearing reverses between e=0 and e=4 μm. At e=0, $\omega_1 < \omega_2$, whereas at e=4 μm $\omega_1 > \omega_2$.

5. Chaotic vibrations

Our results and those of other researchers, such as Tiwari et al. [20], indicate that one or more chaotic attractors can appear in the vibrations of ball bearings as the shaft speed increases depending on the amount of internal clearance in the bearing. Therefore, a comprehensive mapping of the chaotic attractors in the response of the ball bearing requires a systematic study of the response of ball bearings in the internal clearance–shaft speed parameter space.

We start by constructing the bifurcation diagram of the bearing vibrations, Fig. 12, for an arbitrary value of the internal clearance e=7 μm. The diagram is constructed by sampling $\dot{Y}$ at the ball passage frequency $N\omega$ as the shaft speed ω_s was increased from 0 to 3000 rpm. The figure shows multiple chaotic attractors in two shaft speed zones: a zone in the neighbourhood of the horizontal natural frequency stretching from 557 to 2220 rpm and a zone in the neighbourhood of the vertical natural frequency starting at 2723 rpm. The chaotic attractors in the first zone exist in bubble structures bracketed by the cascades of period doubling and reverse period doubling indicated in the figure. The reverse period doubling cascade at ω_s=2220 rpm is shown in Fig. 13. As the shaft speed increases from ω_s=2225 to 2260 rpm, a period 4T orbit gives way to a period 2T orbit. At ω_s=2315 rpm, the period 2T orbit gives birth to a period 1T orbit.

We determined the presence of chaos in the vibrations of the ball bearing by observing the evolution of the bearing vibrations on planar projections of phase-space. Chaotic motions wander in a limited area within the projection plane without closing. Fig. 14 compares the orbits of the shaft motion projected onto the $Y-\dot{Y}$ plane for various internal clearances and a shaft speed of ω_s=3000 rpm. For small internal clearances of e=0 and 3 μm shown in Figs. 14(a) and (b),

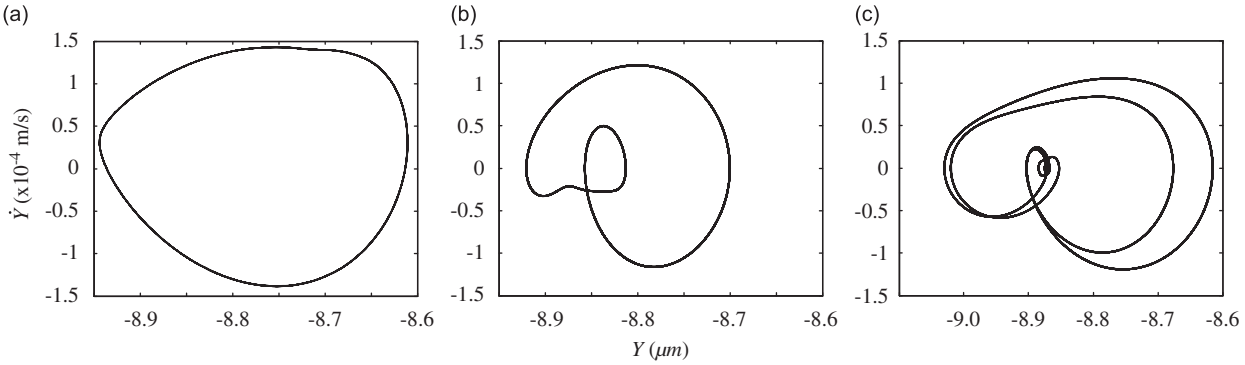

Fig. 13. Reverse period doubling cascade when e=7 μm: (a) period 1T at 2315 rpm, (b) period 2T at 2260 rpm, (c) period 4T at 2225 rpm.

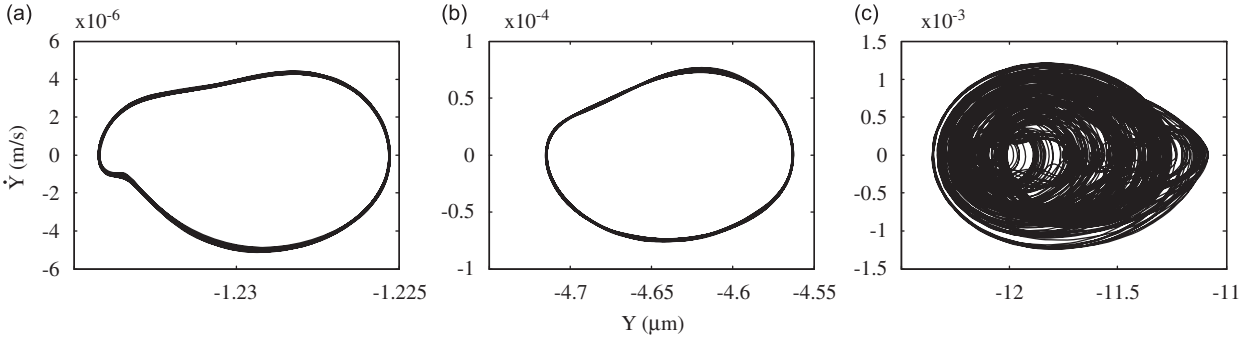

Fig. 14. Phase-portraits of the shaft vertical motions at (a) e=0, (b) e=3 μm, and (c) e=7 μm.

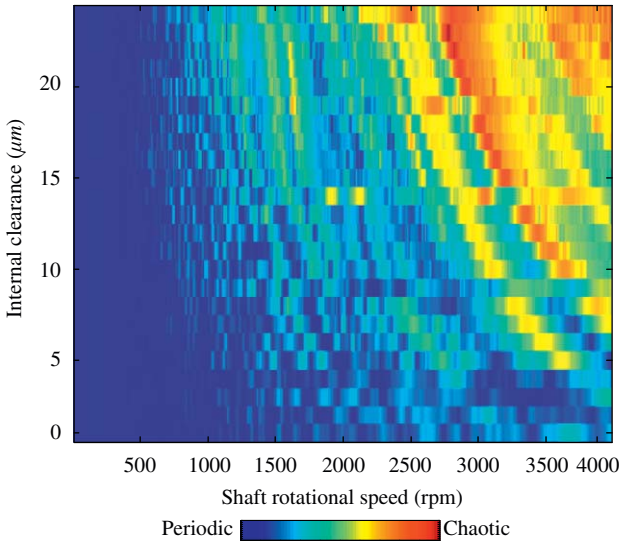

Fig. 15. The chaos map of ball bearing SKF 6204.

respectively, the bearing vibrations are periodic. At the larger internal clearance of $e=7\,\mu m$, corresponding to the rightmost point of Fig. 12, the bearing vibrations are aperiodic filling a limited region of the phase plane and indicating chaos.

To generate the chaos map shown in Fig. 15, the internal clearance was increased from 0 to 24 μm in steps of 1 μm and a bifurcation diagram was constructed at each step. Each bifurcation diagram was then sampled at a constant shaft speed ω_s interval. The results are reported in the chaos map as the size of the chaotic attractor at a pixel in the internal clearance–shaft speed $(e-\omega_s)$ plane using color code. The size of a chaotic attractor is measured as the difference between the maximum and minimum values of $\dot{Y}$ in the bifurcation diagram. Dark blue corresponds to periodic solutions where the attractor size is reported as zero (no chaos). All other colors indicate the presence of chaos, with the color grading indicating the relative size of the chaotic attractor. A qualitative sense of the correspondence between the color grading and the size of the attractor can be obtained by comparing the seventh line of Figs. 15–12. As expected, no chaotic attractors appear for internal clearance values $e>10\,\mu m$ where single-well oscillations preclude the possibility of chaos. On the other hand, the absence of any dark blue pixels in the map for $e>5\,\mu m$ and $\omega_s>3000\,rpm$ shows that chaotic motions dominate the bearing response when the internal clearance is larger than 5 μm and the shaft speed ω_s is higher than 2500 rpm.

6. Conclusions

This work seeks to explain the vibration characteristics of balanced fault-free bearings. We found that the number and location of the equilibrium points of the lumped rotor-shaft mass depends on the internal clearance in the bearing. Bearings with clearance smaller than a critical value $e<e_{cr}$ (class C1) have one stable equilibrium point. This point is located at the vertical symmetry line of the bearing. It translates downward along that line as the clearance increases. For nonzero shaft speeds, the bearing behaves as a self-excited oscillator excited at the ball passage frequency and exhibits a symmetric periodic orbit around this equilibrium point. For larger clearance values, $e>e_{cr}$ (class C2 and higher), three equilibrium points exist: an unstable saddle near the centerline and two stable equilibrium points on either side. The locations of these equilibrium points change over time along an arch composed of a center unstable stretch and two outer stable stretches.

The critical value of internal clearance e_{cr} is a function of the bearing dimensions and structure. For ball bearing SKF6204, we found that critical value to be $e_{cr}=4.5\,\mu m$. As the internal clearance increases past e_{cr}, the equilibrium point undergoes a supercritical pitchfork bifurcation changing the dynamics of the bearing from an oscillator operating in a one-potential well to an oscillator operating in a two-potential wells. At low shaft speeds, the bearing develops single-well (asymmetric) periodic orbits. As the shaft speed increases, two-well orbits appear around the two stable equilibrium points, which keep changing their locations over time resulting in the asymmetric net-like chaotic orbits reported by other researchers. As the shaft speed increases further, two-well periodic orbits develop.

We used the method of averaging to developed closed-form expressions of the frequency-response functions of the bearing horizontal and vertical motions for ball bearings operating in one-potential well $e<e_{cr}$. Specifically, we obtained the frequency-response functions of the ball bearings SKF6204 horizontal and vertical motions at $e=0$ and $4\,\mu m$. Our results indicate that increasing the internal clearance has a softening effect on the bearing stiffness that decreases its vertical and horizontal natural frequencies. We also found that horizontal motions can be assumed uncoupled from

vertical motions but that vertical motions can only be assumed uncoupled from horizontal motions for negligible bearing clearance $e \approx 0$. For small non-zero clearance values, significant energy transfers from horizontal to vertical motions preclude the assumption of uncoupled vertical motions.

For bearings with internal clearance values past the pitchfork bifurcation $e > e_{cr}$, multiple chaotic attractors develop in two zones of the shaft speed ω_s corresponding to the horizontal and vertical natural frequencies of the bearing. The number, frequency range, and size of those attractors increase as the value of the internal clearance and the shaft speed increases. We developed a chaos map to capture the distribution and intensity of chaos in the internal clearance–shaft speed parameter space.

We conclude that the development of a health monitoring system for ball bearings should start from a realization that chaos is not necessarily an indicator of a bearing fault or a shaft-rotor unbalance. Chaos arises *naturally* and *frequently* in balanced fault-free bearings with an internal clearance value beyond the pitchfork bifurcation of the bearing equilibrium point. Therefore, the monitoring system will have to ascertain whether the healthy bearing is operating in a chaotic or periodic regime. For bearings operating in a chaotic region, health monitoring will have to depend on tracking changes in the characteristics of the chaotic attractor rather than the mere existence or lack of chaos.

Acknowledgment

This work was funded by the Natural Sciences and Engineering Research Council of Canada.

Appendix A

Assuming $e=0$, a quasi-static loading condition $\omega_s \approx 0$, and using the polar transformation $x_e = r_e \cos\varphi_e$ and $y_e = r_e \sin\varphi_e$ in Eq. (5) yields

$$\sum_{i=0}^{N/2-1} \left(r_e \cos\left(\varphi_e - \frac{2\pi i}{N}\right)\right)^{1.5} \cos\left(\frac{2\pi i}{N}\right) = 0,$$

$$\sum_{i=0}^{N/2-1} \left(r_e \cos\left(\varphi_e - \frac{2\pi i}{N}\right)\right)^{1.5} \sin\left(\frac{2\pi i}{N}\right) = \frac{W}{k}. \tag{A.1}$$

In the range $[3\pi/2, 2\pi]$, it can be assumed that:

$$\cos^{1.5}\left(\varphi - \frac{2\pi i}{N}\right) \approx \cos\left(\varphi - \frac{2\pi i}{N}\right).$$

When N is an even number larger than 8, trigonometric combinations transform the set of equations into following

$$\frac{N r_e^{1.5} \cos(\varphi_e)}{4} = 0,$$

$$-\frac{N r_e^{1.5} \sin(\varphi_e)}{4} = \frac{W}{k}, \tag{A.2}$$

which results in

$$(x_e, y_e)|_{e=0} = (0, -(4W/Nk)^{2/3}). \tag{A.3}$$

References

[1] O.G. Gustafsson, T. Tallian, Research report on study of the vibration characteristics of bearings, *Technical Report*: AL631023, Reg: 58514:4223 (1963) SKF Inc.
[2] C.S. Sunnersjö, Varying compliance vibrations of rolling bearings, *Journal of Sound and Vibration* 58 (1978) 363–373.
[3] T.E. Tallian, O.G. Gustafsson, Progress in rolling bearing vibration research and control, *ASLE Transaction* 8 (1965) 195–207.
[4] F.P. Wardle, S.Y. Poon, Rolling bearing noise-cause and cure, *Chartered Mechanical Engineer* 30 (1983) 36–40.
[5] H. Shimizu, H. Tamura, Vibration of rotor based on ball bearing—1st report, static stiffness of ball bearing, *Journal of JSME* 9 (1966) 524–532.
[6] H. Tamura, H. Shimizu, Vibration of rotor based on ball bearing—2nd report, static stiffness of ball bearing containing a small number of balls, *Journal of JSME* 10 (1967) 763–775.
[7] H. Tamura, Y. Tsuda, On the spring characteristics of a ball bearing—extreme characteristics with many balls, *Journal of JSME* 23 (1980) 961–969.
[8] L.D. Meyer, F.F. Ahlgren, B. Weichbrodt, An analytic model for ball bearing vibrations to predict vibration response to distributed defects, *Journal of Mechanical Design* 102 (1980) 205–210.
[9] N. Tandon, A. Choudhury, An analytical model for the prediction of the vibration response of ball bearings due to a localized defect, *Journal of Sound and Vibration* 205 (1997) 275–292.
[10] A. Choudhury, N. Tandon, Vibration response of ball bearings in a rotor bearing system to a local defect under radial load, *Journal of Tribology* 128 (2006) 252–261.
[11] N. Akturk, M. Uneeb, R. Gohar, The effects of number of balls and preload on vibration associated with ball bearings, *Journal of Tribology* 119 (1997) 747–753.

[12] N. Akturk, Some characteristic parameters affecting the natural frequency of a rotating shaft supported by defect-free ball bearings, *Journal of Multi-Body Dynamics* 217 (2003) 145–151.
[13] M. Tiwari, K. Gupta, O. Prakash, Dynamic response of an unbalanced rotor supported on ball bearings, *Journal of Sound and Vibration* 238 (2000) 757–779.
[14] M. Tiwari, K. Gupta, O. Prakash, Experimental study of a rotor supported by deep groove ball bearing, *International Journal of Rotating Machinery* 8 (2002) 243–258.
[15] S.P. Harsha, K. Sandeep, R. Prakash, Non-linear dynamic behaviours of rolling element bearings due to surface waviness, *Journal of Sound and Vibration* 272 (2004) 557–580.
[16] S.P. Harsha, P.K. Kankar, Stability analysis of a rotor bearing system due to surface waviness and number of balls, *International Journal of Mechanical Sciences* 46 (2004) 1057–1081.
[17] S.P. Harsha, Nonlinear dynamic analysis of a high-speed rotor supported by ball bearings, *Journal of Sound and Vibration* 290 (2006) 65–100.
[18] E.H. Gad, S. Fukata, H. Tamura, Computer simulation of rotor radial vibration due to ball bearings, *Memoirs of the Faculty of Engineering, Kyushu University* 44 (1984) 83–111.
[19] B. Mevel, J.L. Guyader, Routes to chaos in ball bearings, *Journal of Sound and Vibration* 162 (1993) 471–487.
[20] M. Tiwari, K. Gupta, O. Prakash, Effect of radial internal clearance of a ball bearing on the dynamics of a balanced horizontal rotor, *Journal of Sound and Vibration* 238 (2000) 723–756.
[21] S.P. Harsha, Nonlinear dynamic response of a balanced rotor supported on rolling element bearings, *Mechanical Systems and Signal Processing* 19 (2005) 551–578.
[22] S.H. Ghafari, F. Golnaraghi, F. Ismail, Effect of localized faults on chaotic vibration of rolling element bearings, *Nonlinear Dynamics* 53 (2008) 287–301.
[23] S. Fukata, E.H. Gad, T. Kondou, T. Ayabe, H. Tamura, On the vibration of ball bearings, *Journal of JSME* 28 (1985) 899–904.
[24] F.C. Moon, *Chaotic Vibrations, An Introduction for Applied Scientists and Engineers*, Wiley, New York, 1987.
[25] A.H. Nayfeh, Resolving controversies in the application of the method of multiple scales and the generalized method of averaging, *Nonlinear Dynamics* 40 (2005) 61–102.